JOURNAL OF GEOPHYSICAL RESEARCH, VOL. 114, C02019, doi:10.1029/2008JC005007, 2009

Internal solitary waves induced by flow over a ridge: With applications to the northern South China Sea

Ping-Tung Shaw,[1] Dong Shan Ko,[2] and Shenn-Yu Chao[3]

Received 3 July 2008; revised 11 October 2008; accepted 17 December 2008; published 24 February 2009.

[1] The generation of internal solitary waves by barotropic tides over a ridge is studied in a nonhydrostatic numerical model under idealized oceanographic settings. The experiments examine the effects of ridge width, barotropic tidal strength, and stratification on wave generation. The barotropic tidal flow produces internal wave beams emitting from the ridge top if the slope of the ridge exceeds a critical value equal to the slope of the wave beam. Reflection and refraction of a wave beam in an upper ocean waveguide associated with a strong shallow thermocline produce horizontally propagating internal tides. When the local Froude number over a ridge is not small, lee waves generated on the ridge convert enough energy from the barotropic tides to the internal tides to form tidal bores and solitary waves. Increasing stratification at ridge depths enhances the generation of internal waves, particularly at the diurnal periods. In the Luzon Strait, the slope of the wave beam decreases in spring and summer as stratification at the ridge depths increases, favoring the generation of internal tides. Without the presence of a strong shallow thermocline, internal solitary waves are not observed east of the Luzon Strait. In the northern South China Sea, internal solitary waves are likely observed from April to July when a strong shallow thermocline is present. A deep mixed layer in winter suppresses the production of internal solitary waves.

Citation: Shaw, P.-T., D. S. Ko, and S.-Y. Chao (2009), Internal solitary waves induced by flow over a ridge: With applications to the northern South China Sea, *J. Geophys. Res.*, *114*, C02019, doi:10.1029/2008JC005007.

1. Introduction

[2] Westward propagating internal solitary waves (ISWs) in the northern South China Sea are ubiquitous in satellite images [e.g., *Liu et al.*, 2004] and mooring observations [*Ramp et al.*, 2004]. In the satellite images, these waves travel toward the continental margin southeast of China in the form of long, north–south running crests [e.g., *Liu et al.*, 2004; *Zhao et al.*, 2004] and are reflected and diffracted by the Tung-Sha Island [*Chao et al.*, 2006]. During the passage of ISWs, a westward velocity of 2 m s^{-1} and a thermocline depression of 150 m have been recorded in moored observations [*Ramp et al.*, 2004; *Yang et al.*, 2004]. Most ISWs are first-mode waves with a depression front but second-mode waves have been observed as well [*Yang et al.*, 2004]. The propagation speed, estimated to be 1.5–3.0 m s^{-1}, is close to the phase speed of the first-mode internal waves. A map of the observed ISWs in the northern South China Sea is given by *Zheng et al.* [2007, Figure 2a].

[3] The large vertical isopycnal displacement and the strong horizontal flow induced by ISWs are of concern to marine operations, warranting prediction of the occurrence of these waves. ISWs at many locations in the world ocean are generated by strong barotropic tidal flow over a submarine ridge [e.g., *Vlasenko et al.*, 2005]. In the Luzon Strait, the numerical experiments of *Niwa and Hibiya* [2004] show that M_2 internal tides are effectively generated over two prominent subsurface ridges by the barotropic tides as indicated by the divergence in the integrated internal tidal energy flux. Tracing wave rays in satellite images clearly indicates that the Luzon Strait is the source region of these waves [*Zheng et al.*, 2007]. Using phase speed estimated from climatological stratification, *Zhao and Alford* [2006] further correlate the arrival of ISW packets in the northern South China Sea with the barotropic tidal flow in the Luzon Strait. Amplitude of the ISWs has also been found to correlate with the range of the barotropic tides in the Luzon Strait [*Lien et al.*, 2005].

[4] In the satellite images, ISWs generated in the Luzon Strait propagate westward into the South China Sea. Few or no ISWs are documented over the ridges and to the east of the Luzon Strait. The occurrence of ISWs also depends on season. Statistical analysis shows the ubiquitous presence of ISWs in the northern South China Sea from April to July [*Zheng et al.*, 2007]. If the same oceanic conditions are used on both sides of the Luzon

[1]Department of Marine, Earth, and Atmospheric Sciences, North Carolina State University, Raleigh, North Carolina, USA.
[2]Oceanography Division, Naval Research Laboratory, Stennis Space Center, Mississippi, USA.
[3]Horn Point Laboratory, Center for Environmental Science, University of Maryland, Cambridge, Maryland, USA.

0148-0227/09/2008JC005007$09.00

Strait, numerical simulations [e.g., *Shaw and Chao*, 2006] indicate that ISWs propagate eastward and westward, unable to explain the lack of ISWs east of the Luzon Strait. In addition, how stratification in the northern South China Sea affects the seasonal variation of ISWs needs to be clarified.

[5] Two mechanisms of ISW generation over a ridge have been suggested in the weakly nonlinear theory [e.g., *Helfrich and Melville*, 2006]. In the lee wave generation mechanism [*Maxworthy*, 1979], a depression in the thermocline is first produced in the lee of a ridge by the barotropic tidal flow. As the tide reverses, the depression moves away from the ridge in the direction of the flow to form a rank-ordered solitary wave packet. *Apel et al.* [1985] used this mechanism to describe the ISW generation in the Sulu Sea. The second mechanism is associated with internal tide generation. Fronts develop in large-amplitude internal tides produced by flow over a ridge. Rank-ordered wave packets then form at the wavefronts by nonlinear dispersion [*Lee and Beardsley*, 1974]. *Zhao et al.* [2004] linked the ISW generation in the northern South China Sea to this mechanism. However, observations of the ISWs in the northern South China Sea are unable to differentiate the two mechanisms.

[6] Most ISW theories assume weak nonlinearity and small topography [*Vlasenko et al.*, 2005; *Helfrich and Melville*, 2006]. In the South China Sea, the thermocline depression associated with the ISWs is large, and ridges in the Luzon Strait occupy a good fraction of the water depth. Beyond weak nonlinearity and small topography, this study simulates ridge-generated internal tides and their transformation to ISWs in a nonhydrostatic numerical model under idealized conditions. This work is part of a larger project sponsored by the Office of Naval Research. The project includes field observations, remote sensing, theoretical studies, and numerical efforts with a goal to develop scientific understating that leads to a predictive capability of ISWs. Toward this goal, this process study features the oceanic conditions favoring the development of ISWs in the northern South China Sea. Restricting our goal as such, the simulations do not purposely reproduce the quantitative aspects of ISW properties, e.g., the observed wave amplitude and the distance from the ridge where nonlinear ISWs first appear.

[7] The organization of this paper is as follows. Section 2 briefly reviews the model formulation. Results from the simulation are given in Section 3. From the simulation results, optimal conditions for the generation of ISWs are discussed in Section 4 and summarized in Section 5. It is found that prediction of ISWs requires knowledge of the barotropic tides and stratification at the ridges in the Luzon Strait as well as the upper ocean stratification in the northern South China Sea.

2. Model Description

[8] The three-dimensional nonhydrostatic numerical model of *Shaw and Chao* [2006] is used in this study. *Chao et al.* [2006, 2007] have employed this model in earlier studies of ISWs in the northern South China Sea. The model uses three-dimensional momentum, continuity, and density equations with Boussinesq and rigid lid approximations. The governing equations are

$$\frac{D\mathbf{v}}{Dt} + 2\Omega\mathbf{k}' \times \mathbf{v} = -\frac{1}{\rho_0}\nabla p - \frac{\rho}{\rho_0} g\mathbf{k} + A\nabla_H^2\mathbf{v} + \nu\frac{\partial^2\mathbf{v}}{\partial z^2}, \quad (1)$$

$$\nabla \cdot \mathbf{v} = 0, \text{ and} \quad (2)$$

$$\frac{D\rho}{Dt} = K\nabla_H^2\rho + k\frac{\partial^2\rho}{\partial z^2}, \quad (3)$$

where $\mathbf{v}$ is the three-dimensional velocity vector (u, v, w) in the (x, y, z) coordinate, $\mathbf{k}'$ is a unit vector pointing upward from the North Pole, $\mathbf{k}$ is the local upward unit vector, ρ is the density after removing a reference value ρ_0(=1028 kg m^{-3}), Ω is the Earth's rotation rate, and p is the pressure. The eddy viscosity and diffusivity are constant, so that $A = K =$ 4 m^2 s^{-1}, $\nu = 1 \times 10^{-4}$ m^2 s^{-1}, and $k = 0.1 \times 10^{-4}$ m^2 s^{-1}. Equation (1) includes both the horizontal and vertical components of the Coriolis acceleration, and the traditional approximation of neglecting the vertical Coriolis acceleration is not used.

[9] The finite difference form of the governing equations and the solution procedure are described by *Shaw and Chao* [2006]. A brief outline is given here. The Arakawa-C grid system is used for the spatial discretization of equations (1), (2), and (3). Vertical discretization follows the z coordinate formulation. Spatial derivatives are center differenced to second-order accuracy. Integration in time follows the Adams-Bashforth scheme. At each time step, the baroclinic pressure, barotropic pressure, and nonhydrostatic pressure are computed separately. The baroclinic pressure is calculated by vertically integrating the right-hand side of the z momentum equation. Setting the divergence of the horizontal transport to zero then produces a two-dimensional Poisson equation for the barotropic pressure. The equation is solved by matrix inversion. A three-dimensional Poisson equation is derived for the nonhydrostatic pressure by taking the divergence of equation (1) and setting it to zero using equation (2). The equation is solved by iteration using the preconditioned conjugate gradient method [e.g., *Pozrikidis*, 1997].

[10] The experiments were carried out in a channel at 20°N, the latitude of the Luzon Strait. The x axis is toward east along the channel axis, and the channel depth is chosen to be 800 m for simulation of internal waves in the upper ocean. A "bell-shaped" ridge, uniform in y direction, is placed at x = 0 km. The ridge height h is given by

$$h = \frac{h_m}{1 + (x/L)^2}, \quad (4)$$

where h_m and L are the maximum height and the scale width of the ridge, respectively. In this study, h_m = 600 m, and the top of the ridge is 200 m below sea surface. The scale width L varies from 15 km to 60 km (Table 1). The west and east boundaries are located at x = −200 and 200 km, respectively. Two grid cells are used in the y direction. A

Table 1. List of Experiments in this Study[a]

Experiment	L (km)	N_0 (rad s^{-1})	u_0 (m s^{-1})	Phase Speed (m s^{-1})
1a	15	0.015	0.1	1.52
1b	30	0.015	0.1	1.52
1c	45	0.015	0.1	1.52
1d	60	0.015	0.1	1.52
2a	45	0.015	0.2	1.52
2b	60	0.015	0.2	1.52
3a	15	0.008	0.1	0.76
3b	30	0.008	0.1	0.76
4a	30	0.015[b]	0.1	1.48
4b	30	0.015[c]	0.1	1.05

[a]The scale width of the ridge (L) is defined in equation (4), and the buoyancy frequency (N_0) is given by equation (7). The amplitude of barotropic tides is u_0. The last column is the phase velocity of the first mode wave in deep water away from the ridge.
[b]Mixed layer ($N = 2 \times 10^{-4}$ rad s^{-1}) in the upper 50 m.
[c]Mixed layer ($N = 2 \times 10^{-4}$ rad s^{-1}) in the upper 150 m.

periodic condition in y results in solutions with no y variation, effectively running a two-dimensional simulation in a three-dimensional model. The vertical grid size is 10 m, and the horizontal grid size is 200 m.

[11] The density field consists of ambient vertical stratification $\rho_a(z)$ and the perturbation density anomaly $\rho'(x, z)$:

$$\rho = \rho_a(z) + \rho'(x, z). \tag{5}$$

[12] Except for the mixed layer, the ambient stratification is given by

$$\rho_a(z) = -\frac{\Delta\rho}{2}\left[1 + \tanh\left(\frac{z - z_0}{D}\right)\right], \tag{6}$$

where $\Delta\rho$ is the density scale. The center of the thermocline is at depth z_0(=−50 m), and the thickness of the thermocline is given by D(=120 m). The buoyancy frequency is

$$N = [-(g/\rho_0)d\rho_a/dz]^{1/2} = \left(\frac{g\Delta\rho}{2\rho_0 D}\right)^{1/2} \cosh^{-1}\left(\frac{z - z_0}{D}\right)$$
$$= N_0 \cosh^{-1}\left(\frac{z - z_0}{D}\right). \tag{7}$$

[13] In most cases (Experiments 1 and 2), $\Delta\rho$ is chosen to be 6 kg m^{-3}, resulting in a maximum buoyancy frequency $N(z = z_0) = N_0 = 0.015$ rad s^{-1}. Figure 1a shows vertical profiles of density and buoyancy frequency. The first three normal modes for horizontal velocity and perturbation density, calculated by solving the eigenvalue problem numerically, are plotted in Figures 1b and 1c, respectively. The zero crossing depth for the mode 1 horizontal velocity (also the depth of maximum density perturbation) is 200 m. The phase speeds of the first three baroclinic modes are 1.52, 0.64 and 0.41 m s^{-1} in the deep water, respectively. Over the ridge top, the local phase speed for the mode 1 wave is calculated to be 0.89 m s^{-1} using the local water depth.

[14] Radiation conditions for the first-mode baroclinic wave are adopted at the open boundaries at $x = -200$ and 200 km. A rigid lid is used on the surface for computational efficiency. Because of the vast difference in phase speed (1.5 m s^{-1} for baroclinic waves versus 90 m s^{-1} for barotropic waves), imposing the rigid lid approximation should not affect the amplitude and phase speed of internal tides over the ridge significantly. No normal flow conditions are used on all solid boundaries, and a no-slip condition dictates the tangential velocity on the bottom. Tidal forcing is included by specifying the sinusoidal barotropic inflow/outflow velocity on the two x boundaries. The tidal current starts from zero at $t = 0$ as an ebb tide with eastward flow. In most experiments, the maximum tidal velocity on open boundaries (u_0) is 0.1 m s^{-1}. Although the semidiurnal tides are used in all experiments to facilitate discussion, similar conclusions can be extended to diurnal tides. All experiments use a time step of 31.05 s, which is 1/120 of the semidiurnal tidal period (12.42 hours). All experiments run for five tidal cycles.

[15] Table 1 shows four sets of experiments conducted in this study. The first set (Experiments 1a to 1d with Experiment 1b as the control run) examines the sensitivity of ISW generation to the ridge width or L. The second set (Experiments 2a to 2b) increases the barotropic tidal speed twofold using two ridge widths. The third set (Experiments 3a to 3b) deviates from the first set by halving the buoyancy frequency in the water column using two ridge widths. In the fourth set (Experiments 4a to 4b), a mixed layer is imposed at the surface.

3. Results

3.1. Internal Wave Generation

[16] ISWs are associated with sharp depression fronts, strong downward flow, and convergent surface currents. Among them, contour plots of the u velocity in the numerical result give the best visual effects to identify ISWs. Figure 2 shows snapshots of u velocity contours between 2.5 and 3 tidal cycles after initialization for Experiment 1b, the control run. In this time span, the barotropic tidal current is to the left or negative. In the Luzon Strait, this would be the flood phase of the semidiurnal tidal current. As the flood tide intensifying from 31.05

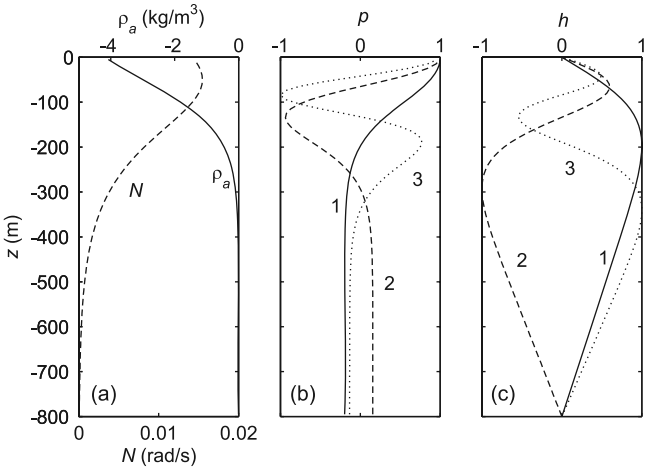

Figure 1. (a) Density ρ_a in kg m^{-3} and buoyancy frequency N in rad s^{-1} in Experiments 1 and 2. The corresponding normal modes are shown (b) for horizontal velocity and (c) for density perturbation. The phase speeds are 1.52, 0.64, and 0.41 m s^{-1} for the first three modes.

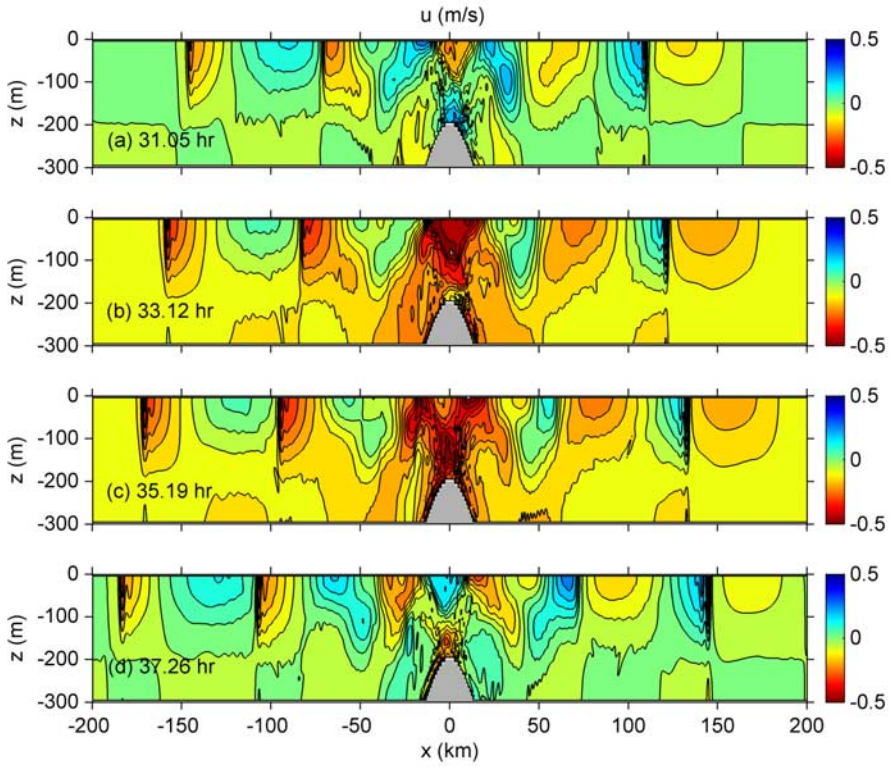

Figure 2. Contour plots of u velocity in m s^{-1} for Experiment 1b at (a) 31.05, (b) 33.12, (c) 35.19, and (d) 37.26 hours during the flood tide (barotropic tidal flow to the left). The contour interval is 0.05 m s^{-1}.

hours to 33.12 hours, two slanting wave beams of strong westward flow extend upward from a point over the ridge top. In the bands, contour lines, which are also constant phase lines, move downward from 33.12 hours to 35.19 hours, indicating upward energy propagation along internal wave beams. Some energy also propagates downward from the ridge top along both faces of the ridge. Similar wave beams are displayed in the internal wavefield generated by an oscillating point source in the classical laboratory experiments of *Mowbray and Rarity* [1967; see *Gill*, 1982, p. 137]. Thus, internal waves in Figure 2 are produced by the tidal current over the top of the ridge. Reflection of the wave beams by the surface at $x = -15$ km is clearly seen at 35.19 hours (Figure 2c). The stronger one of the two upward wave beams is on the downstream side of the ridge. The particle speeds on top of the ridge in Figure 2 are less than 0.5 m s^{-1}, which gives a moderate local Froude number about 0.5 for a phase speed of 0.89 m s^{-1}. *Vlasenko et al.* [2005] concluded that nonlinear effects do not play a dominant role in the generation of internal tides over inclined bottom topography at low Froude numbers.

[17] The two wave beams, reflected downward by the sea surface, are refracted upward at $x = -30$ km as they enter deep water with decreasing stratification. After zigzagging, the upper ocean waveguide transforms the wave to horizontally propagating shallow water waves in the hydrostatic regime. For example, the first-mode baroclinic wave structure is established on the left side of the ridge after the second reflection from the surface (to the left of $x = -60$ km in Figure 2a). Intensification of wavefronts occurs quickly thereafter. For example, a tidal bore is clearly seen at $x = -71$ km in Figure 2a. Six hours later, the tidal bore develops into a rank-ordered, internal solitary wave train at $x = -110$ km (Figure 2d). To its left is another tidal bore generated one tidal cycle earlier.

[18] On the left side of the ridge, a tidal bore forms on the leading edge of a negative velocity region. At generation, negative u velocity is associated with the flood tides. Thus, the two wave trains on the left side of the ridge in Figure 2 were generated when the barotropic flow on the ridge top changed from ebb to flood tides during the first two tidal cycles. On the right side of the ridge, the corresponding tidal bores appear on the leading edge of a region of positive u velocity and are associated with the beginning of ebb tides at generation.

[19] Contour plots of perturbation density provide more insights into the wave generation mechanism (Figure 3). At the slack water before the flood tide (hour 31.05), the isopycnal has been depressed downward on the right (lee) side of the ridge by an earlier ebb tide (Figure 3a). Above the ridge, isopycnals are depressed along a path toward left following a wave beam in Figure 2a. As the barotropic tide turns toward left (Figure 3b), the signal in isopycnal depression is reflected by the surface as in Figure 2. The first-mode structure in isopycnal depression appears at 37.26 hours (Figure 3d). This depression will eventually intensify similar to the one at $x = -94$ km produced one tidal cycle earlier in Figure 3c. Figure 3 shows that westward propagating internal tidal bores originate from lee waves produced by the ebb tide on the east side of the

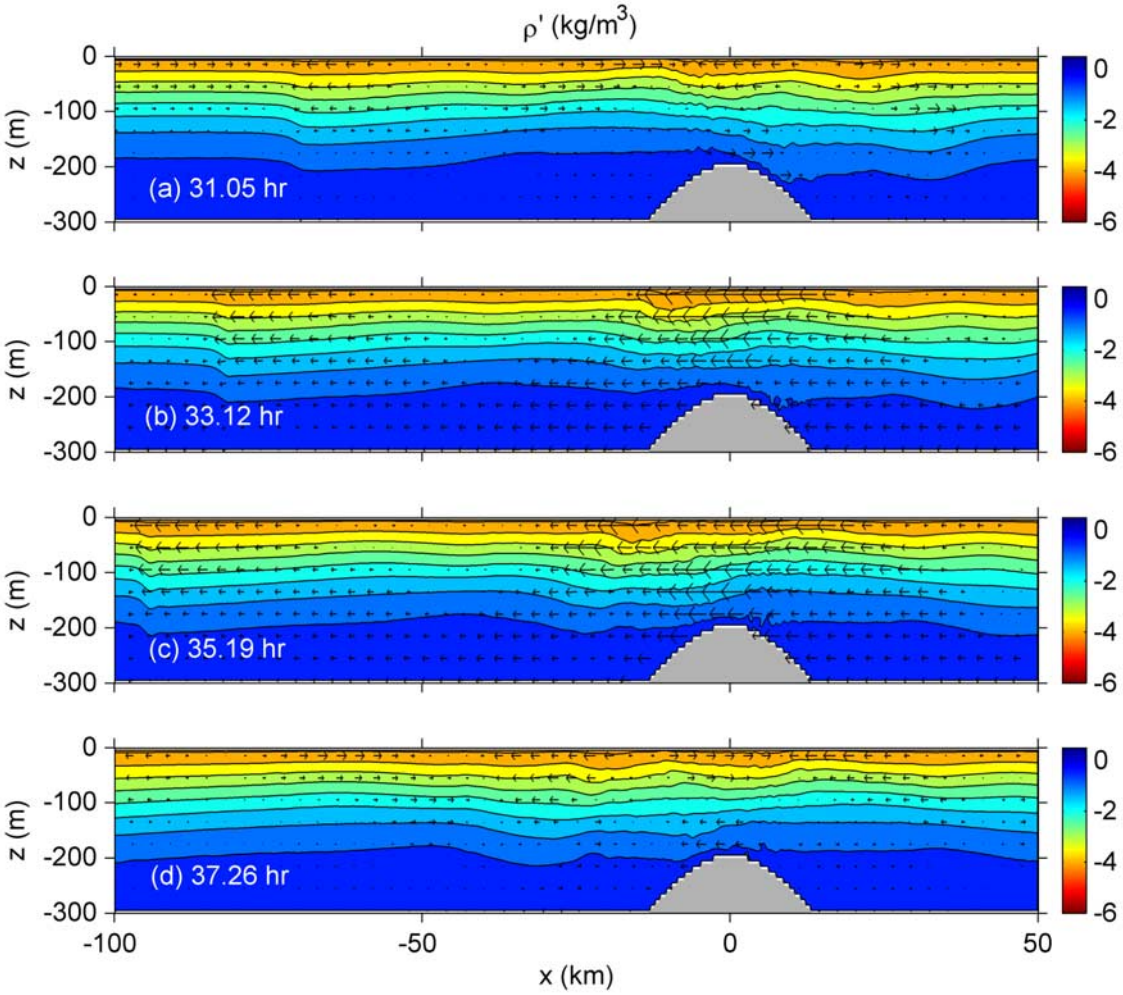

Figure 3. Contour plot of perturbation density (ρ') in kg m^{-3} for Experiment 1b at (a) 31.05, (b) 33.12, (c) 35.19, and (d) 37.26 hours during the flood tide. The contour interval is 0.5 kg m^{-3}. The maximum velocity is 0.5 m s^{-1} for u and 0.01 m s^{-1} for w.

ridge. Tidal bore generation can be traced back to the start of a flood tide, in agreement with the timing inferred from Figure 2.

3.2. Formation of Internal Solitary Waves

[20] In Experiment 1b, ISWs eventually develop in a tidal bore, e.g., at $x = -180$ km and -110 km in Figure 2d. Contours of perturbation density ρ' and the velocity vectors associated with a well-developed solitary wave train at hour 43.37 from Experiment 1b are shown in Figure 4. The leading depression is at $x = -142$ km with an amplitude of 30 m, followed by a smaller depression at $x = -138$ km. The tidal phase corresponds to the slack water before the flood tide. The barotropic flow vanishes at this time, and the (u, w) velocity vector represents the flow field of the solitary wave. The structure is described by the first baroclinic mode (Figure 1). The maximum speed at the surface is 0.4 m s^{-1} and is located at $x = -142$ km, the position of the maximum depression. The distance between the first two wave troughs is 3.6 km. Strong convergence produces downward motion about 0.6 km ahead of the maximum horizontal velocity at the front, followed by alternating upward and downward motion. The maximum downward velocity is 0.01 m s^{-1}. The magnitude decreases rapidly behind the front.

[21] Propagation of internal waves at $z = -5$ m is shown in the contour plot of the u velocity on the x-t plane (Figure 5). Patches of minima and maxima in the u velocity contours along parallel slanting lines show outward wave propagation from the ridge top at $x = 0$ km. The horizontal bands are produced by the alternating barotropic tidal current. Since the data are stored every hour, the crowded contour lines at a wavefront cannot be fully resolved, producing small, wavy patches. On the left (right) side of the ridge, the leading edge of a region of negative (positive) u velocity intensifies to form a bore. Propagation of ISWs on the left (right) side of the ridge can be traced back to the beginning of the flood (ebb) phase of the barotropic tides over the ridge top. The timing is consistent with the analysis in Section 3.1 and that by *Zhao and Alford* [2006]. Estimated from the slope of the position of each wavefront on the x-t plane, the propagation speed of the internal bores is fairly constant at 1.65 ± 0.07 m s^{-1}, or about 6 km h^{-1}. This

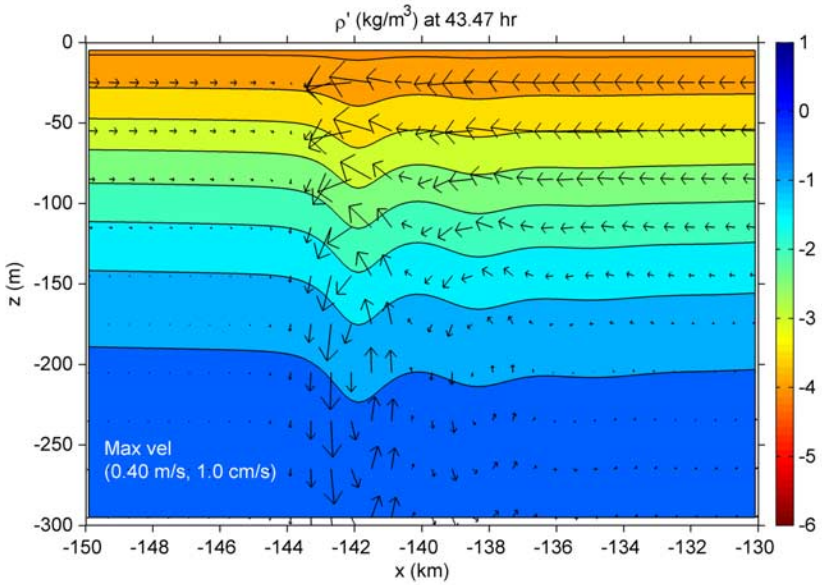

Figure 4. Perturbation density contours and the velocity vector in the *x*-*z* plane, showing a well-developed solitary wave train at 43.47 hours in Experiment 1b. Contour values are from −4 to −0.5 kg m^{-3} at a contour interval of 0.5 kg m^{-3}. The maximum velocity is 0.4 m s^{-1} for *u* and 0.01 m s^{-1} for *w*.

value is higher than the theoretical value of 1.52 m s^{-1} for the first baroclinic waves. Nonlinear effects clearly increase the speed of wave propagation.

3.3. Effect of the Ridge Width

[22] Figure 6 shows contour plots of the *u*-velocity at the end of the third tidal cycle (t = 37.26 hours) for ridges with different width scales (Experiments 1a, 1b, 1c, and 1d). Internal wave beams exist near the ridge in all panels, but the wave strength decreases with increasing ridge width. In all cases, vertically propagating waves evolve to first-mode shallow water waves about 100 km away from the ridge because of wave reflection and refraction. The first-mode waves then intensify to form ISWs in Figures 6a and 6b. When L increases to 45 km (Figure 6c), internal waves still emit from the ridge but the wavefront at $x = -100$ km shows only slight intensification. At $x = -170$ km, the trough produced one tidal cycle earlier is strongly dissipated (Figure 6c). Little internal wave energy leaves the ridge when L is further increased to 60 km (Figure 6d). Thus, the strength of the baroclinic tides depends on the ridge steepness. Energy is converted from the barotropic tide to the baroclinic tide if the ridge steepness exceeds a critical value.

[23] Table 2 shows the first three local extremes in *u* velocity associated with left-propagating waves in Figure 6. The peak velocities at the two tidal bores ($x = -180$ and -110 km) are given by u_1 and u_3, while u_2 is the maximum positive velocity in between ($x = -130$ km). These values describe the amplitude of the baroclinic wave at t = 37.26 hours when the barotropic tidal velocity is zero. In particular, u_1 and u_3 are the troughs in the baroclinic flow generated during the first two flood phases of the barotropic tides, and u_2 is the peak speed generated during the second ebb tide (Figure 5). The last column indicates the presence of ISWs in the experiment. When ISWs form (Experiments 1a and 1b), the value of u_2 is higher than the maximum barotropic flow (0.1 m s^{-1}). Furthermore, u_1 and u_3 are much greater than u_2 because of intensification of the wavefronts. Experiment 1c is near the borderline of ISW formation. With a weak front at $x = -100$ km, u_2 and u_3 are about the same as the barotropic tidal velocity, but u_1 is smaller. In Experiment 1d, the baroclinic velocity u_2 is 0.06 m s^{-1} or 2/3 of the barotropic velocity, while u_1 and u_3 are about half of u_2. In this case, no ISWs form. Multiple troughs are usually associated with the ISWs, e.g., between $x = -180$ and -190 km in Figure 6a. The average wavelengths, estimated from the distance of the first two consecutive troughs, are 4 km and 3 km, for u_1 and u_3, respectively. Similar values have been reported in the observed ISWs [e.g., *Ramp et al.*, 2004]. Thus, surface

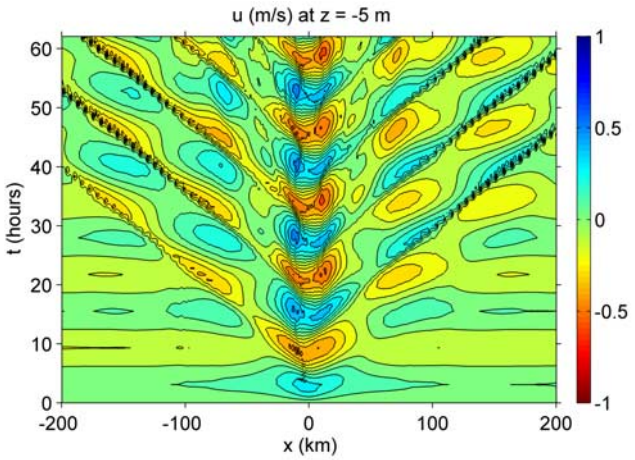

Figure 5. Contour plot of *u* velocity at $z = -5$ m on the *x*-*t* plane for Experiment 1b. The contour interval is 0.1 m s^{-1}. The ridge peak is at x = 0 km.

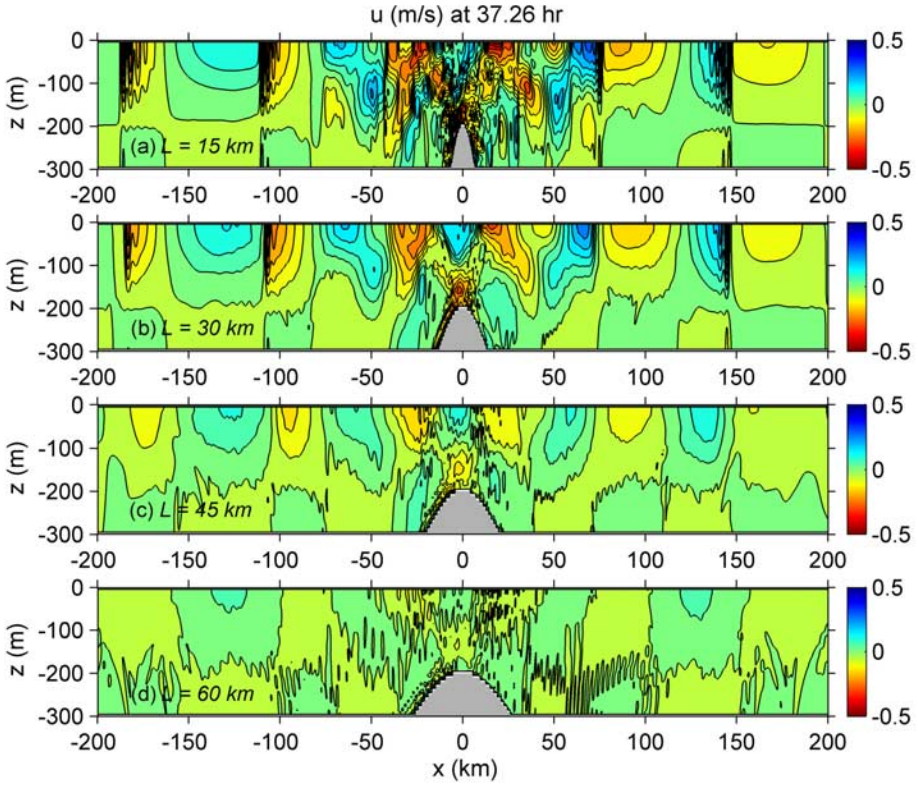

Figure 6. Contour plots of u velocity at slack water before flood tide at t = 37.26 hours for four scale widths of the ridge (L): (a) 15 km, (b) 30 km, (c) 45 km, and (d) 60 km. The contour interval is 0.05 m s^{-1}.

convergence with velocity much greater than the maximum barotropic tidal current is a telling sign of the presence of ISWs.

[24] If the barotropic velocity in Experiment 1c is doubled to 0.2 m s^{-1}, sharp fronts form in Experiment 2a (Figure 7a). Compared to the values in Experiment 1c, u_2 is nearly doubled (0.19 m s^{-1}), but u_1 and u_3 are three times that in Experiment 1c (Table 2), indicating ISW formation. When the barotropic velocity in Experiment 1d is doubled, u_1, u_2, and u_3 in Experiment 2b increase proportionally with all three values much lower than the barotropic flow (Table 2). No wavefronts form in this case (Figure 7b). In Experiments 2a and 2b, the maximum barotropic tidal velocity is 0.8 m s^{-1} on top of the ridge. With a local phase speed of 0.89 m s^{-1}, the local Froude number is close to 1. Increase in the strength of lee waves as the Froude number approaching 1 may explain why ISWs appear in Experiment 2a, in which the ridge slope is near the critical value. However, for a slope below the critical value as in Experiment 2b, ISWs are not generated even the Froude number is near 1.

3.4. Stratification

[25] In the linear internal wave theory, the slope of the wave beam in an ocean with constant buoyancy frequency N_0 is

$$\tan\phi = \sqrt{(\omega^2 - f^2)/(N_0^2 - \omega^2)} \qquad (8)$$

where ϕ is the angle between the wave beam and the horizontal axis, ω is the wave frequency, and f is the Coriolis parameter [e.g., *Gill*, 1982, p. 259]. Thus, the critical ridge slope is inversely proportional to N_0 at tidal frequencies. Experiments 3a and 3b parallel Experiments 1a and 1b, respectively, except for a twofold reduction of the buoyancy frequency throughout the water column. From equation (8), the critical slope in Experiments 3a and 3b is twice that in Experiments 1 and 2. The phase speeds for the first two normal modes are reduced to 0.76 and 0.32 m s^{-1}, respectively, and the Froude number is about 1 for mode 1 waves in both Experiment 3a and 3b. The contour plot of u velocity in Experiment 3a shows multiple troughs trailing the wavefront (Figure 7c). In Table 2, the speeds at the crest (u_1 and u_3) are more than twice that at the trough (u_2), which is slightly higher than the barotropic tidal speed (u_0).

Table 2. First Three Local Extremes in the Velocity of the Left-Propagating Waves at t = 37.26 h[a]

Experiment	u_0 (m s^{-1})	u_1 (m s^{-1})	u_2 (m s^{-1})	u_3 (m s^{-1})	ISW?
1a	0.1	−0.36	0.15	−0.40	Yes
1b	0.1	−0.29	0.15	−0.31	Yes
1c	0.1	−0.08	0.11	−0.12	No
1d	0.1	−0.04	0.06	−0.03	No
2a	0.2	−0.29	0.19	−0.37	Yes
2b	0.2	−0.10	0.13	−0.07	No
3a	0.1	−0.27	0.13	−0.32	Yes
3b	0.1	−0.05	0.06	−0.03	No
4a	0.1	−0.22	0.14	−0.24	Yes
4b	0.1	Unidentifiable	Unidentifiable	Unidentifiable	No

[a]The maximum barotropic tidal flow is u_0. The baroclinic velocities are given by u_1, u_2, and u_3. The last column indicates whether ISW is generated in each experiment.

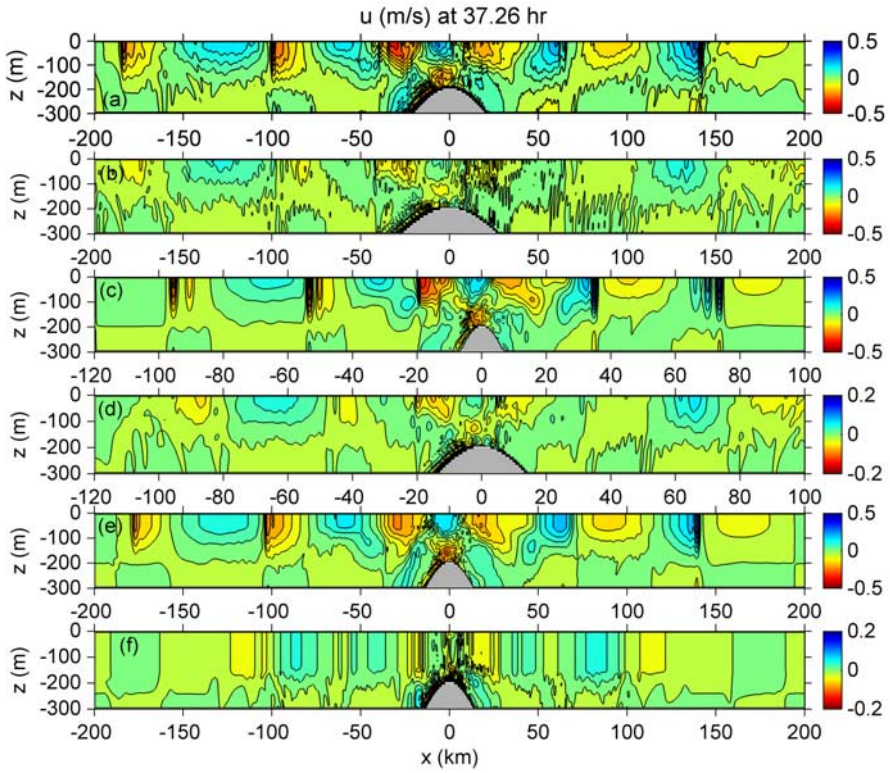

Figure 7. Contour plots of u velocity at slack water before flood tide at t = 37.26 hours for (a) Experiment 2a, (b) Experiment 2b, (c) Experiment 3a, (d) Experiment 3b, (e) Experiment 4a, and (f) Experiment 4b. The contour interval is 0.05 m s^{-1} in all cases except 0.02 m s^{-1} in Figures 7d and 7f.

ISWs are generated in this case. The wave amplitude is only slightly lower than that in Experiment 1a (Table 2).

[26] If L in Experiment 3a is doubled (Experiment 3b), only weak internal waves propagate away from the ridge (Figure 7d). The internal waves are so weak that ISWs no longer develop. The u velocity in Experiment 3b is qualitatively different from that in experiment 1b. The speed at the trough in Experiment 3b is lower than the barotropic tidal speed, indicating no wavefront formation (Table 2). The speed at the trough is also lower than that at the crest as expected. Again, the ridge slope must exceed a threshold to convert sufficient energy from the barotropic tides to internal tides for ISW formation even the Froude number is close to 1.

[27] Experiments 4a and 4b use the same stratification as in Experiment 1b but the upper ocean now contains a mixed layer 50 and 150 m deep, respectively. The mixed layer is weakly stratified with a buoyancy frequency of 2 $\times$ 10^{-4} rad s^{-1}, allowing internal waves at the semidiurnal frequency to exist in the mixed layer. The first-mode phase speeds decrease to 1.48 m s^{-1} and 1.05 m s^{-1} in Experiments 4a and 4b, respectively. In Figure 7e, solitary wave trains appear in the u velocity field at hour 37.26; development of ISWs is not affected by the presence of a shallow mixed layer. The extreme velocities in Table 2 show some reduction in peak velocities u_1 and u_3 though. If the mixed layer depth increases to 150 m, the mixed layer effectively erases the thermocline at $z = -50$ m shown in Figure 1a. Internal wave propagation is hardly seen (Figure 7f). Another experiment has been conducted to further distinguish the role of the thermocline in ISW generation. The stratification in the top 300 m of the water column in Experiment 1b is replaced by one with constant buoyancy frequency (N = 0.015 rad s^{-1}). The thermocline is diffused over the top 300 m, but the maximum buoyancy frequency is unchanged. The result (not shown) contains only linear hydrostatic internal waves propagating away from the ridge, pointing out the need of a sharp thermocline to trap wave beams for ISW generation.

4. Discussion

[28] Barotropic tides over a ridge generate internal tides propagating away from the ridge top in slanting wave beams. Away from the ridge, an upper ocean waveguide at the buoyancy frequency maximum (Figure 1a) traps internal waves because of wave reflection and refraction. Wave propagation eventually becomes horizontal some distance away from the ridge. The strength of the internal tides is crucial to the development of tidal bores and ISWs. Significant energy is converted from the barotropic tides to the internal tides only when the ridge slope exceeds a critical value. Thus, a steep ridge would be most efficient in generating internal tides in the ocean. Linear theory [e.g., *Hurley and Keady*, 1997] and laboratory experiments [e.g., *Zhang et al.*, 2007] suggest that internal wave generation is possible when the ridge slope exceeds the slope of the wave beam. The numerical experiments in section 3 validate this

criterion when the flow is nonlinear and the ridge height is a large fraction of the water depth. If the ridge slope is less than the critical value, only weak internal waves are produced.

[29] Tidal bores, if formed, are always located on the leading edge of the down-wave surface flow. In the northern South China Sea, westward propagating ISWs are associated with the leading edge of the westward flow in the upper ocean. At generation, the westward surface baroclinic flow occurs when the barotropic tidal flow over the ridge changes from ebb (eastward) to flood (westward). The analysis by *Zhao and Alford* [2006] shows that ISWs in the northern South China Sea are associated with westward barotropic tides in the Luzon Strait. The numerical result is consistent with the observed wave behavior.

[30] Equation (8) gives the critical slope as a function of wave frequency and buoyancy frequency. The wave beam becomes more horizontal as the buoyancy frequency increases. Thus, strong stratification at ridge depths favors generation of baroclinic tides. Furthermore, the internal wave beam is more horizontal at the diurnal period than at the semidiurnal period under the same stratification. A ridge is therefore more likely to become supercritical for diurnal tides than for semidiurnal tides although simulations of diurnal tides are not explicitly illustrated in this study. *Ramp et al.* [2004] observed strong ISWs at the diurnal period in this region (their 24-hour or type a waves). Diurnal barotropic tides are stronger than the semidiurnal tides in the Luzon Strait, but a supercritical ridge slope for the diurnal tides may also contribute to the difference in amplitude of internal waves.

[31] The discussion based on linear theory holds when the local Froude number on the ridge top is much less than 1. In the linear wave limit, two symmetrical wave beams emit from the ridge top. Lee waves are produced over a large-amplitude obstacle by barotropic oscillatory flow in the Froude number range between 0.5 and 1.75 in the laboratory and numerical experiments of *Matsuura and Hibiya* [1990]. Westward propagation of depressed isopycnals in Figure 3 (Froude number $\sim$ 0.5) is consistent with the lee wave theory. During the ebb tide, isopycnals are depressed on the east side of the ridge because of energy accumulation by internal waves propagating against the eastward tidal current. As the tidal current reverses to the west, the depression propagates westward over the ridge to enhance the wave beam on the left side of the ridge. Large amplitude internal waves occur at Froude number $\sim$ 1 over a narrow ridge in the experiments of *Matsuura and Hibiya* [1990]. The Froude number is affected by the strength of the tidal current and the local phase velocity over the ridge top. *Zhao and Alford* [2006] rejected the lee wave mechanism on the basis of the lack of eastward flow immediately before the westward flow that produces ISWs. However, by examining their Figure 8, a period of deceleration and acceleration always appears in the westward current even if two ISW-producing peaks in the westward current are not separated by eastward flow. It is likely that two consecutive westward bursts of lee waves are released in one diurnal cycle as a response to mixed semidiurnal and diurnal tidal forcing. The lee wave bursts, originating from a depression produced on the east side of the ridge by the previous eastward tidal flow, are separated by decelerating and accelerating tides rather than eastward flow.

[32] It seems that both lee waves and internal tides play a role in the ISW generation. The ridge slope controls the generation of linear internal tides from a ridge but energy needed to form nonlinear ISWs has to come from lee waves. Thus, ISW generation requires a supercritical slope as well as a Froude number close to 1 over the ridge top. For a ridge slope greater than the critical value, internal waves are generated and may evolve into nonlinear ISWs if the Froude number is not too small. The local Froude number does not constitute an overbearing criterion for ISW generation though. ISWs are not generated when the ridge slope is less than the critical value even when the local Froude number is close to one.

[33] Development of ISWs involves not only the conversion of energy from the barotropic tides to the baroclinic tides but also the formation of horizontally propagating internal waves at the thermocline [*Gerkema*, 2001; *Akylas et al.*, 2007]. Thus, generation of ISWs is a two-step process. First, internal wave beams are produced by the barotropic tides over a ridge. This step requires a supercritical ridge slope and a Froude number that is not too small. In the second step, an upper ocean waveguide produced by a sharp thermocline is needed to trap internal wave energy. Large-amplitude internal tides are produced if the thermocline is sharp; subsequent nonlinear intensification in the internal tides leads to the formation of tidal bores and ISWs. Without a strong thermocline, only linear internal waves propagate away from the ridge. A shallow upper ocean mixed layer does not affect the formation of ISWs, but a deep mixed layer that erases the sharp thermocline would prevent the development of ISWs.

[34] The Kuroshio, flowing northward along a path east of the Luzon Strait, is a boundary between the warm water in the Philippine Sea and the colder subsurface water in the South China Sea. The thermocline is noticeably deeper on the east side of the Kuroshio than in the South China Sea. The position of the Kuroshio affects the stratification at ridge depths in the Luzon Strait and thus internal wave generation. The surface position of the Kuroshio has been studied [e.g., *Yuan et al.*, 2006], but few observations on the variation of its subsurface boundary are available. Therefore, the climatology data are used to describe the change in stratification. The monthly buoyancy frequency distribution at 400 m depth near the Luzon Strait in Figure 8 is constructed from the Navy Ocean Climatology Database (GDEM version 3.0), which is compiled from observed temperature and salinity profiles. The buoyancy frequency increases from the South China Sea to the Philippine Sea, ranging from 0.0061 rad s^{-1} (3.5 cycles h^{-1}) in dark blue to 0.0079 rad s^{-1} (4.5 cycles h^{-1}) in dark red. Two ridges are present in the Luzon Strait: the east ridge following the island chain to the east and the west ridge extending southward from the southern tip of Taiwan. In Figure 8, stratification at ridge depths is stronger from March to August than the rest of the year. According to the numerical simulation in Section 3, spring and summer should be the favorite period for the generation of internal wave beams.

[35] Figure 9, also from the Navy Ocean Climatology Database, shows mean vertical profiles of density and buoyancy frequency on the two sides of the Luzon Strait

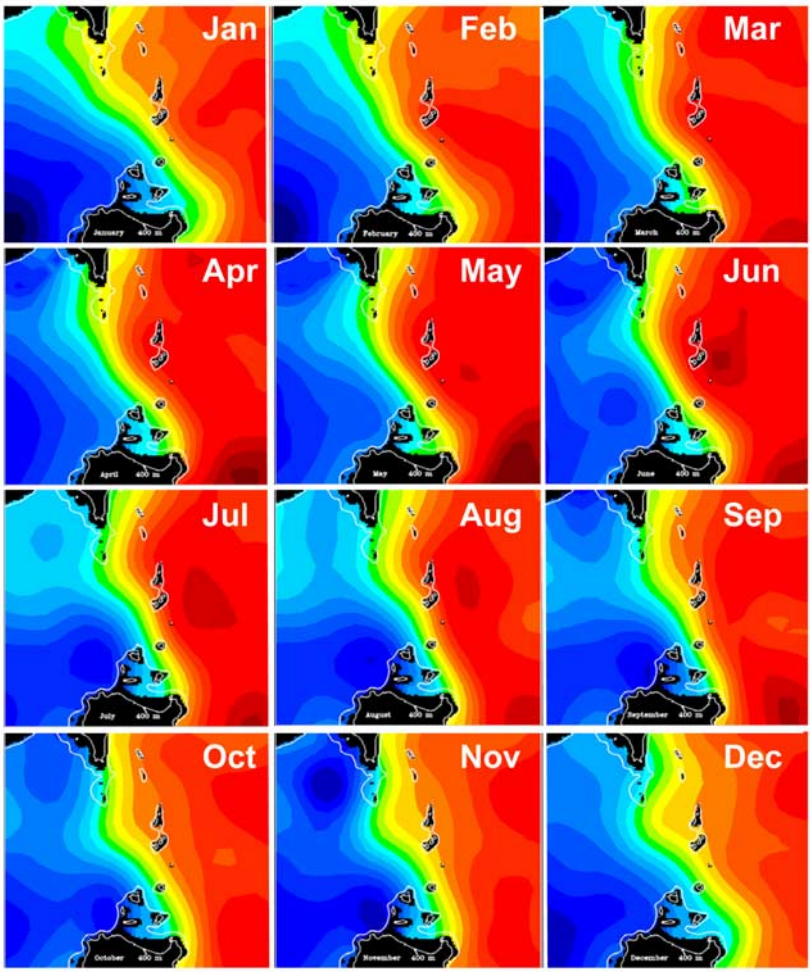

Figure 8. Monthly mean buoyancy frequency at 400 m in the Luzon Strait. The color varies progressively from dark blue at 3.5 cycles h^{-1} (0.0061 rad s^{-1}) to dark red at 4.5 cycles h^{-1} (0.0079 rad s^{-1}). The islands at top and bottom of Figure 8 are Taiwan and Luzon, respectively.

between April and June. The left panel indicates that the thermocline is stronger and shallower on the west side than on the east side of the Luzon Strait. The buoyancy frequency profile in the right panel shows higher values below 150 m on the east side of the Luzon Strait than in the South China Sea, consistent with Figure 8. Because the steeper, taller east ridge is more likely in waters of stronger stratification than the west ridge; the east ridge is likely the major source of ISWs in the northern South China Sea. The buoyancy frequency profiles also show a shallow layer of high buoyancy frequency in the South China Sea but not east of the Luzon Strait. Missing an upper ocean waveguide associated with a strong, shallow thermocline may explain the lack of ISWs east of the Luzon Strait.

[36] The shallow thermocline in the northern South China Sea favors ISW formation; a deep mixed layer weakens the thermocline and thus hinders the ISW formation. Local cooling and wind-induced mixing may produce a mixed layer, but intrusion of surface water from the Philippine Sea in winter [*Shaw*, 1991; *Yuan et al.*, 2006] effectively erases the sharp thermocline. *Qu et al.* [2007, Figure 10] calculated the monthly depth of the isothermal surface that coincides with the base of the mixed layer in the South China Sea. In the region west of Luzon Strait, the mixed layer depth decreases from January to June and then increases to a maximum in November. The shallowest mixed layer occurs from April to

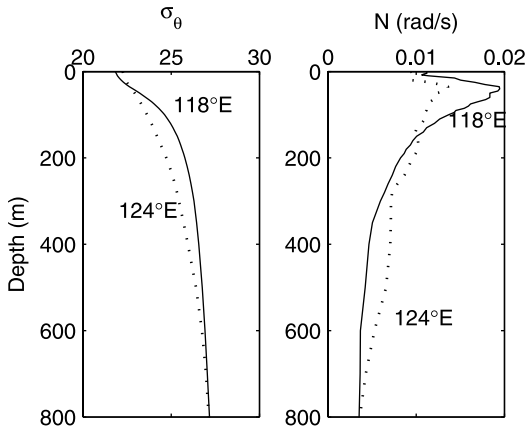

Figure 9. Vertical profiles of mean density (left) and buoyancy frequency (right) averaged over April–June at 20°N, 118°E (solid line) and at 20°N, 124°E (dot line).

August, a favorite period for ISW formation as predicted by the present study and in the study of *Zhao and Alford* [2006].

5. Conclusions

[37] The numerical experiments in this study identify the process crucial to the formation of ISWs in the northern South China Sea. The model can be fine-tuned to match the observed parameters, e.g., the amplitude of ISWs, the distance where nonlinear ISWs begin to form, etc., but it is not the intention of this paper. Rather, ISW generation by the barotropic tides is demonstrated in the simplest model configuration. The oceanographic conditions that may affect ISW generation are identified and are applied to the northern South China Sea.

[38] Generation of ISWs is a two-step process. First, internal wave beams are produced in the Luzon Strait by the barotropic tides over ridges with supercritical slopes. The critical value for slope is determined by stratification, which is in turn affected by the position of the Kuroshio. The stronger stratification at 400 m in spring and early summer near the ridges in the Luzon Strait may enhance the conversion from barotropic energy to baroclinic energy. The energy conversion favors diurnal tides over semidiurnal tides. The ridge slope controls the generation of linear internal tides from a ridge but energy needed to produce large-amplitude internal tides comes from lee waves. If the Froude number is not too small on a supercritical ridge, lee waves enhance the westward propagating internal tides to form tidal bores and ISWs.

[39] The second step of ISW generation requires a sharp thermocline to trap energy in vertically propagating wave beams to form horizontally propagating internal tides. When the thermocline is diffuse or erased by the presence of a deep mixed layer, horizontally propagating internal tides are weak, and no ISWs form. A shallow upper ocean mixed layer above the thermocline does not affect ISW formation. The mixed layer southwest of Taiwan is shallow from April to August. Not surprisingly, satellite observations reveal ubiquity of ISWs during this period. ISWs are mostly absent east of the Luzon Strait, where a sharp upper ocean thermocline is missing.

[40] **Acknowledgments.** The authors would like to thank two anonymous reviewers, whose comments inspire further insights into the generation mechanism. The research is supported by the Office of Naval Research of the U.S. Navy under contracts N00014-05-1-0280 (Shaw), N00014-08WX-2-0930 (Ko), and N00014-05-1-0279 (Chao). This is UMCES contribution 4236.

References

Akylas, T. R., R. H. J. Grimshaw, S. R. Clarke, and A. Tabaei (2007), Reflecting tidal wave beams and local generation of solitary waves in the ocean thermocline, *J. Fluid Mech.*, *593*, 297–313, doi:10.1017/S0022112007008786.

Apel, J., J. R. Holbrook, A. K. Liu, and J. J. Tsai (1985), The Sulu Sea Internal Soliton Experiment, *J. Phys. Oceanogr.*, *15*, 1625–1651, doi:10.1175/1520-0485(1985)015<1625:TSSISE>2.0.CO;2.

Chao, S.-Y., P.-T. Shaw, M.-K. Hsu, and Y.-J. Yang (2006), Reflection and diffraction of internal solitary waves by a circular island, *J. Oceanogr.*, *62*, 811–823, doi:10.1007/s10872-006-0100-4.

Chao, S.-Y., D.-S. Ko, R.-C. Lien, and P.-T. Shaw (2007), Assessing the west ridge of Luzon Strait as an internal waves mediator, *J. Oceanogr.*, *63*, 897–911, doi:10.1007/s10872-007-0076-8.

Gerkema, T. (2001), Internal and interfacial tides: Beam scattering and local generation of solitary waves, *J. Mar. Res.*, *59*, 227–255, doi:10.1357/002224001762882646.

Gill, A. E. (1982), *Atmosphere-Ocean Dynamics*, Academic, San Diego, Calif.

Helfrich, K. R., and W. K. Melville (2006), Long nonlinear internal waves, *Annu. Rev. Fluid Mech.*, *38*, 395–425, doi:10.1146/annurev.fluid.38.050304.092129.

Hurley, D. G., and G. Keady (1997), The generation of internal waves by vibrating elliptic cylinders. Part 2. Approximate viscous solution, *J. Fluid Mech.*, *351*, 119–138, doi:10.1017/S0022112097007039.

Lee, C. Y., and R. C. Beardsley (1974), Generation of long nonlinear internal waves in a weakly stratified shear-flow, *J. Geophys. Res.*, *79*, 453–462, doi:10.1029/JC079i003p00453.

Lien, R.-C., T. Y. Tang, M. H. Chang, and E. A. D'Asaro (2005), Energy of nonlinear internal waves in the South China Sea, *Geophys. Res. Lett.*, *32*, L05615, doi:10.1029/2004GL022012.

Liu, A. K., S. R. Ramp, Y. Zhao, and T. Y. Tang (2004), A case study of internal solitary wave propagation during ASIAEX 2001, *IEEE J. Oceanic Eng.*, *29*, 1144–1156, doi:10.1109/JOE.2004.841392.

Matsuura, T., and T. Hibiya (1990), An experimental and numerical study of the internal wave generation by tide topography interaction, *J. Phys. Oceanogr.*, *20*, 506–521, doi:10.1175/1520-0485(1990)020<0506:AEANSO>2.0.CO;2.

Maxworthy, T. (1979), A note on the internal solitary waves produced by tidal flow over a three-dimensional ridge, *J. Geophys. Res.*, *84*, 338–346, doi:10.1029/JC084iC01p00338.

Mowbray, D. E., and B. S. H. Rarity (1967), A theoretical and experimental investigation of the phase configuration of internal waves of small amplitude in a density stratified fluid, *J. Fluid Mech.*, *28*, 1–16, doi:10.1017/S0022112067001867.

Niwa, Y., and T. Hibiya (2004), Three-dimensional numerical simulation of M2 internal tides in the East China Sea, *J. Geophys. Res.*, *109*, C04027, doi:10.1029/2003JC001923.

Pozrikidis, C. (1997), *Introduction to Theoretical and Computational Fluid Dynamics*, 675 pp., Oxford Univ. Press, Oxford, U.K.

Qu, T., Y. Du, J. Gan, and D. Wang (2007), Mean seasonal cycle of isothermal depth in the South China Sea, *J. Geophys. Res.*, *112*, C02020, doi:10.1029/2006JC003583.

Ramp, S. R., T. Y. Tang, T. F. Duda, J. F. Lynch, A. K. Liu, C.-S. Chiu, F. L. Bahr, H.-R. Kim, and Y.-J. Yang (2004), Internal solitons in the northern South China Sea. Part I: Sources and deep water propagation, *IEEE J. Oceanic Eng.*, *29*, 1157–1181, doi:10.1109/JOE.2004.840839.

Shaw, P.-T. (1991), The seasonal variation of the intrusion of the Philippine seawater into the South China Sea, *J. Geophys. Res.*, *96*, 821–827, doi:10.1029/90JC02367.

Shaw, P.-T., and S.-Y. Chao (2006), A nonhydrostatic primitive-equation model for studying small-scale processes: An object oriented approach, *Cont. Shelf Res.*, *26*, 1416–1432, doi:10.1016/j.csr.2006.01.018.

Vlasenko, V., N. Stashchuck, and K. Hutter (2005), *Baroclinic Tides: Theoretical Modeling and Observational Evidence*, Cambridge Univ. Press, London.

Yang, Y.-J., T. Y. Tang, M. H. Chang, A. K. Liu, M.-K. Hsu, and S. R. Ramp (2004), Solitons northeast of Tung-Sha Island during the ASIAEX pilot studies, *IEEE J. Oceanic Eng.*, *29*, 1182–1199, doi:10.1109/JOE.2004.841424.

Yuan, D. L., W. Q. Han, and D. X. Hu (2006), Surface Kuroshio path in the Luzon Strait area derived from satellite remote sensing data, *J. Geophys. Res.*, *111*, C11007, doi:10.1029/2005JC003412.

Zhang, H. P., B. King, and H. L. Swinney (2007), Experimental study of internal gravity waves generated by supercritical topography, *Phys. Fluids*, *19*, doi:10.1063/1.2766741.

Zhao, Z., and M. H. Alford (2006), Source and propagation of internal solitary waves in the northern South China Sea, *J. Geophys. Res.*, *111*, C11012, doi:10.1029/2006JC003644.

Zhao, Z., V. Klemas, Q. Zheng, and X.-H. Yan (2004), Remote sensing evidence for baroclinic tide origin of internal solitary waves in the northeastern South China Sea, *Geophys. Res. Lett.*, *31*, L06302, doi:10.1029/2003GL019077.

Zheng, Q., R. D. Susanto, C.-R. Ho, Y. T. Song, and Q. Xu (2007), Statistical and dynamical analysis of generation mechanisms of solitary internal waves in the northern South China Sea, *J. Geophys. Res.*, *112*, C03021, doi:10.1029/2006JC003551.

S.-Y. Chao, Horn Point Laboratory, Center for Environmental Science, University of Maryland, Cambridge, MD 21613-0775, USA.

D. S. Ko, Oceanography Division, Naval Research Laboratory, Stennis Space Center, MS 39529, USA.

P.-T. Shaw (corresponding author), Department of Marine, Earth, and Atmospheric Sciences, North Carolina State University, Raleigh, NC 27695-8208, USA. (pt_shaw@ncsu.edu)